Visco-frictional trapping of particles percolating through a submerged granular medium

Pierre Philippe, Florian Brunier-Coulin, Yacine Khidas

Visco-frictional trapping of particles percolating through a submerged granular medium

Pierre Philippe*
INRAE, Aix Marseille University, RECOVER, Aix-en-Provence, France.

Florian Brunier-Coulin†
Aix Marseille University, CNRS, Centrale Marseille, IRPHE, Marseille, France.

Yacine Khidas‡
Univ Gustave Eiffel, Ecole des Ponts, CNRS, Navier, Marne-la-Vallée, France.
(Dated: March 6, 2026)

Particle filtration through a porous medium is a much-studied field because of its numerous industrial or natural applications, particularly for deep-bed and cake-type filtration regimes. The percolation regime has received relatively less attention and corresponds to the continuous motion of particles in a porous environment under the principal effect of gravity and generally without any interaction other than contact with the porous matrix. In the present case, both the moving particles and the porous medium are composed of spherical particles of diameters d and D, respectively. Dry percolation has been analyzed under such conditions and exhibits lateral diffusion, as well as a constant mean transit velocity that scales with $\sqrt{gD}$ (with D the coarse grain diameter and g gravity). The behavior is significantly different in the case studied here, where the porous stack is fully saturated by a liquid at rest. A previous study experimentally investigated the transition from deep filtration to the percolation regime under laminar flow conditions by matching the refractive index of the liquid to that of the particles of the porous system [1]. Here, based on the same experimental technique, we focus on the particular case where there is no fluid flow and identify a different type of particle trapping, in contrast with either dry condition or liquid flow situation. We show that this capture, which can exhibit high metastability, stems from a combination of solid friction and viscous lubrication, which strongly reduces the velocity of the moving particles and can also suppress any rebound. The complementary roles of the packing structure and both the size and shape of the particles are also highlighted.

I. INTRODUCTION

There are many practical situations that involve transit through a porous matrix of suspended particles in a fluid, each bringing its own specific set of related problems. Such examples, encountered in both industrial and natural environments, include treatment of wastewater by filtration [2–4], processing of petroleum products [5, 6], intrusion of pollutants or microplastics into soils [7, 8], sediment and slurry clogging in gravel beds [9–13], internal erosion of hydraulic embankments [14, 15].

Considering more specifically injection, migration and clogging of particles in a granular bed, with respective characteristic sizes d (mobile particles) and D (static grains), different filtration regimes are successively encountered depending on the size ratio $\delta = d/D$ [11, 13]. Initially, caking and surface colmation occur due to geometrical obstruction when the particles are too large to find their way between the coarse grains of the porous substrate. Then, by progressively decreasing either the particle size or the size ratio, the so-called deep filtration regime is reached, where transit through constrictions is possible with localized instances of either individual obstruction of a restricted opening or collective particle bridging at narrow pore throats. For smaller particles (or equivalently larger size ratios), the full percolation regime is characterized by unimpeded infiltration under gravity or driven by fluid flow. However, for even finer particles, typically below a few microns, a new class of retention occurs at this small scale, with potential clogging caused by various bio-physico-chemical mechanisms [16–18], such as adsorption and adhesion due to molecular or electrostatic forces, to which Brownian effects must be added. Moreover, in practical applications, a porous filter is often fed with particles by a fluid flow. This induces additional hydrodynamic forces, which can substantially impact the previous micro-scale interactions or lead to mechanical blocking at constrictions.

The scope of the present study concerns exclusively unimpeded percolation regime in submerged hydrostatic condition where bio-physico-chemical interactions on the mobile particles are negligible. Regarding the geometric condition governing the percolation of small particles through a particulate porous medium, grain size distributions of both the coarse grains constituting the bed and the fine percolating particles play a major role. In the fields of hydraulic structures or sediment transport, several empirical filter laws have been proposed, based on various characteristic sizes assumed to satisfactorily

* pierre.philippe@inrae.fr
† florian.brunier-coulin@univ-amu.fr
‡ yacine.khidas@univ-eiffel.fr

represent the overall geometry of the pore space [14, 19]. More recent studies have refined this type of criterion on the so-called opening size of a filter by exploring the constriction size distributions using numerical modeling with the Discrete Elements Method (DEM) [20–23]. In the greatly simplified configuration where the coarse grains are spheres of the same diameter D, the size of the narrowest constriction comes from an ordered local arrangement and can be determined analytically. The corresponding diameter ratio between this smallest constriction and the large particles, sometimes referred to as the Apollonian ratio, is $\delta_c = 2/\sqrt{3} - 1 \approx 0.155$ [23, 24] and roughly delineates the transition from clogging to percolation regimes for intruders [1, 24–27].

Several studies have investigated fine particle trajectories in this percolation regime, mostly in the dry case with air at rest. A significant lateral dispersion of a diffusive nature and a quasi-steady transit velocity U_t, which scales with a characteristic ballistic velocity, was first evidenced by experiments [24, 28, 29], later confirmed by theory [30], and subsequently validated through numerical modeling of percolation using either the Discrete Element Method (DEM) [31–37] or few older geometry-based kinematic simulations [38–40]. Size ratio (δ), restitution and solid friction coefficients (e and μ_s), and packing fraction (ϕ) appear solely as second-order parameters through the following dimensionless relation [24, 28–30, 32, 40]:

$$\frac{U_t}{\sqrt{gD}} = f(\delta, \mu_s, e, \phi) \tag{1}$$

The normalization velocity $\sqrt{gD}$ represents the characteristic velocity acquired by a particle in free fall through a pore, whose median size is known to be proportional to the typical bed grain diameter D. The effect of friction appears to be more marginal, while a decrease in the dimensionless percolation velocity with size ratio δ has been observed [24, 35, 40]. In the case of quasi-elastic rebounds (i.e. when e tends to 1), a theoretical calculation by Wilkinson and Edwards [30] suggests that $U_t/\sqrt{gD}$ scales as $(1-e)^{\frac{1}{4}}$, which appears rather consistent with some previous experimental and numerical data [32, 40]. A recent numerical study conducted with a coefficient of restitution $e = 0.8$ proposes the following global scaling: $U_t \propto \phi^{-1}\sqrt{gD/\delta}$ [35]. This scaling was further validated with a smaller value of $e = 0.3$ and consequently a different prefactor [37].

Several major differences arise, however, when porous percolation occurs in a viscous interstitial liquid. Firstly, another characteristic velocity must be considered, as free-fall regime is generally no longer reached in practice: natural candidates are the viscous settling velocity, as long as the liquid remains almost at rest, or the Darcy velocity in the presence of a porous flow. Secondly, as viscosity increases, bouncing is progressively inhibited, eventually being completely suppressed due to lubrication in the solid contact zone. To account for such collision of particles in fluids, Stokes number St, which compares particle inertia to viscous drag, was proposed as the pertinent dimensionless group, defined in this context as $\mathrm{St} = \rho_p u_p d/(9\mu)$ [41–43], where ρ_p and u_p are respectively the particle density and velocity, and μ is the fluid viscosity. Indeed, consistent experimental results [42, 43] show that the ratio e/e_{dry} between submerged and dry restitution coefficients reduces with decreasing Stokes numbers St. More specifically, and as illustrated with the experimental data by Gondret and co-authors [43] in Figure 1, the dependence of St on the coefficient of restitution e shows a progressive decrease down to a critical value St_c, typically around 10, below which e remains perfectly null, thereby corresponding to fully damped collisions. Very similar results were obtained by Joseph and co-authors [42]. Interestingly, Wilkinson and Edwards proposed long ago a so-called "slither" analytical model for such an inelastic percolation and showed that the lateral diffusion of particles should then become almost negligible in this situation [30].

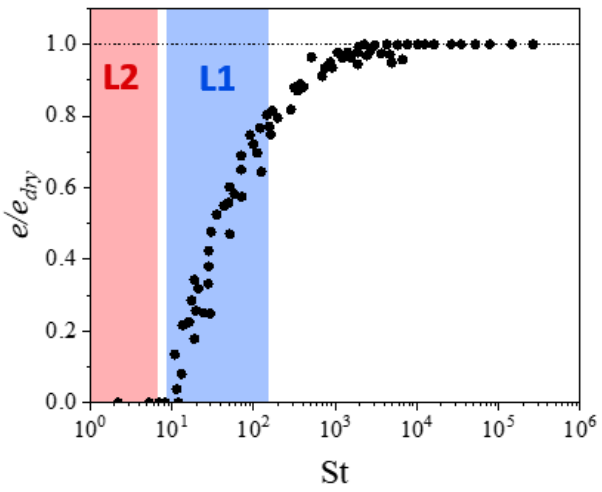

FIG. 1. Coefficient of restitution e normalized by its value in air e_{dry} as a function of the Stokes number St based on data extracted from [43]. Coloured areas represent the approximate ranges in Stokes numbers for the present experiments with liquid L1 where 9 <St< 156 (in blue) and with liquid L2 where 1 <St< 7 (in red).

However, there are only a few previous experiments on submerged deep bed filtration [1, 25, 44–46], almost all under constant liquid discharge conditions, and some more recent simulations based mainly on the coupling between Computational Fluid Dynamics (CFD) and DEM [47–52].

To further investigate the submerged filtration regime of unimpeded percolation in the absence of any geometric obstruction, we have developed an experimental setup enabling visualization and spatio-temporal tracking of particles moving through an immersed granular bed of static spheres. All the experimental aspects are presented in Sec. II, while Sec. III reports on the results obtained, successively detailing the general phenomenology and the evidence of substantial particle trapping despite the ab-

sence of steric hindrance, with the main features highlighted, particularly meta-stability. More specifically, in Sec. IV, various experiments reveal that friction and viscous lubrication together play crucial roles in enabling this entrapment. These experimental results also emphasize the importance of the geometric structure of the grain packing, especially in ordered arrangements, and the intricate influence of the mobile particle size. The article concludes with a comprehensive summary of this visco-frictional trapping, for which a number of outstanding questions remain.

II. EXPERIMENTAL SET-UP AND PROTOCOL

The principle of the experiments consists in tracking the trajectories of small opaque particles within an immersed porous environment made translucent by optical index matching.

A. Granular packing with Refractive Index Matching implementation

As already mentioned, the porous media considered in this study is solely composed of packed grains, restricted to the case of mono-size spheres. In order to achieve an optical matching with an interstitial liquid, we chose borosilicate glass beads with a rather low refractive index of $n = 1.472$. These beads, branded Silibeads type P (provided by Sigmund and Lindner), have high sphericity, good transparency and high stiffness (Young modulus of 64 GPa). In the various experiments carried out throughout this study, two surface finishes could be tested, matt and polished, and the bead diameters used range between 7 and 16 mm. In particular, most of our granular packs are composed of polished beads of diameters 7.3 ± 0.3 mm and 9.7 ± 0.3 mm.

The bead packs are built in a rectangular glass container of dimension 250 mm (height), 150 mm (length), and 100 mm (width). To prevent bead ordering from the walls and to obtain proper random structure inside the packing, a temporary partition wall is used in most cases. The interior of the partition is first filled through a funnel with beads of a given diameter, while the peripheral interstice is completed with a single layer of beads of another diameter as sketched in Figure 2. The partition wall is then slowly removed from the bead stack. This method allows reproducible formation of disordered mono-size packings (except in the direct vicinity of the container walls), of height in the range 16-18 cm and with a volume fraction ϕ measured around 0.62.

As presented later in Sec. IV C, a small number of additional tests are carried out with ordered packs carefully assembled by hand with similar polished spherical beads of borosilicate glass (Silibeads by Merck). More precisely, a centered cubic (CC) structure with 10 mm beads and a face-centered cubic (FCC) structure with 16 mm beads were assembled, reaching volume fractions rather close to the corresponding theoretical values, i.e. $\phi \approx 0.67$ ($\phi_{cc} = 0.68$) and $\phi \approx 0.71$ ($\phi_{fcc} = 0.74$), respectively.

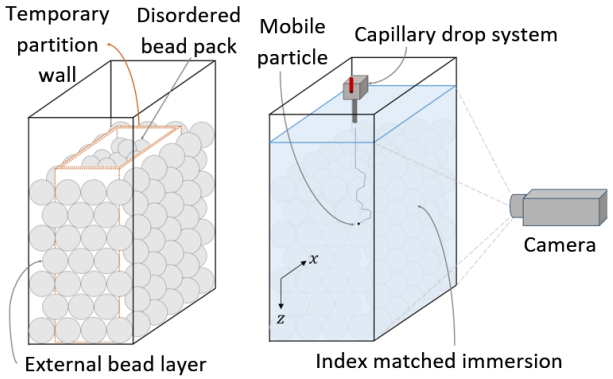

FIG. 2. Diagrams illustrating (left) the method for constructing a disordered spherical bead pack by inserting a temporary partition wall to build an external mono-size bead layer of different diameter, and (right) the release of an opaque particle and its subsequent trajectory through the index-matched porous medium.

As illustrated in Figure 2, the final step in achieving a translucent porous medium is to saturate the bead pack with a liquid of the same refractive index as the beads, thereby minimizing the refraction of light through the two-phase medium. This Refractive Index Matching (RIM) technique has already been implemented, notably to analyze the micro-structure of a granular medium under shear [53–55] or during its hydro-mechanical destabilization [56, 57]. It has also been applied in the present context, especially to study the infiltration of fine particles in a porous bed under seepage fluid flow [1, 25, 44, 45].

Here, we specifically chose two liquids with differnt viscosities that satisfy the RIM condition with an optical index tuned to $n = 1.472$ at the laboratory ambient temperature around 23°C. Liquid L1 is composed (by mass) of 95.7% of dimethylsulfoxide (supplied by Sigma-Aldrich) and 4.3% of distilled water. Liquid $L2$ is a mixture (by mass) of 86% of a light mineral oil (supplied by Sigma-Aldrich) and 14% of an immersion oil (supplied by Cargille). The measurements of density and viscosity (with a falling ball viscometer) of both liquids at 23°C provide: $\rho_1 = 1095$ kg.m^{-3} and $\mu_1 = 2.0$ cP for liquid L1; $\rho_2 = 841$ kg.m^{-3} and $\mu_2 = 21$ cP for liquid L2.

Saturation of the bead pack is achieved by gravity-driven drainage of the RIM liquid from a reservoir at a very low flow rate through a small flexible tube positioned at one corner of the container. This prevents the formation of bubbles that would compromise transparency. Filling is stopped when the liquid level is about 4 cm above the top of the bead pack. As will be shown later, this liquid gap allows the percolating particles to reach, or nearly reach, their terminal settling velocity before entering the porous medium.

B. Protocol and post processing

Thanks to the transparency of our saturated model granular medium, it is possible to track the trajectory of an opaque particle as it passes through it. These mobile particles are also chosen to be spherical, with their maximum diameter limited by the smallest constriction sizes imposed by the random packing geometry. However, to be detected, they cannot be too small compared to the spatial resolution of our camera. We therefore used spherical beads in the global range of diameter $400 < d < 1500$ μm. Most of the experiments were carried using zirconium beads (ZetaBeads provided by Netzsch), with high sphericity and a density $\rho_p = 6000$ kg.m^{-3}. Some prior experiments were conducted with painted glass beads (Decobeads provided by Sigmund Lindner), of density 2500 kg.m^{-3}.

A mass release protocol was tested in a few preliminary experiments with the painted glass beads, before moving on to an individual drop protocol mainly used here. Mass release was obtained by generating a rain of particles, a few centimeters above the liquid surface, manually fed by a gentle flow through a funnel and passing through a grid. These experiments provided the benefit of highlighting the general phenomenology of filtration in the percolation regime, which will be detailed in Sec. III, and in particular the unexpected occurrence of particle trapping despite the absence of individual geometrical obstruction for these sizes of particles. This last point prompted us to modify the protocol to eliminate any collective effects such as particle bridging or straining.

Each individual release test corresponds to the individual tracking of a single percolating zirconium bead in transit through the porous medium. It is possible to reconstruct the trajectory and kinematics of each mobile particle, and then carry out a statistical analysis by reproducing the process a large number of times for many similar particles. Actually, as shown in Figure 3, the particles are released three at a time, with initial positions to the left (L), middle (M) and right (R) of the cell. Given that the trajectories are only slightly deviated laterally, this helps to save time generating neither collision or interaction between particles, nor exploration of the near-wall zone, whose geometry is very different due to the packing construction method.

In more detail, the protocol is as follows. First, each of the three beads is pictured by a camera mounted on a microscope lens, then named according to its subsequent release position (L, M or R) and to the experiment number. Based on the *ImageJ* shape description tools, these close-up photographs of the particle projected areas allow to determine precisely the diameter d of each particle and check its degree of circularity, which remains within the range 0.8-0.9. Non-standard shapes can thus be eliminated. Next, the beads are released simultaneously by a capillary drop system as depicted on the right sketch in Fig. 2. It consists of a total of three capillary tubes holding pendant drops by depression. Each bead is brought into contact with a drop and thus retained by surface tension. The system is then gently lowered until contact with the liquid pool, releasing the particles. Compared with the case where the beads are dropped in the air above the liquid interface (by collective mass release or particle by particle with a tweezers), this protocol allows better control of the release, with low initial velocity, quasi-vertical trajectory, minimal spin drift and great synchronisation of the three particles. After each experiment, the porous medium is cleaned by systematically passing a long metal rod back and forth horizontally inside the packing to remove any trapped particles. This cleaning process also preserves the randomness and volume fraction of the granular packing.

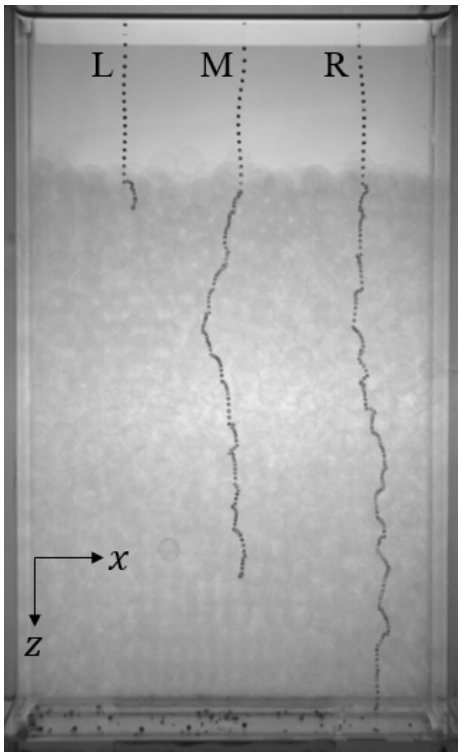

FIG. 3. Percolation of three particles of diameter $d \approx 1.2$ mm released simultaneously from left (L), middle (M) and right (R) sections in the cell, with corresponding trajectories (by projection in the observation plane) above and inside the porous medium made of $D = 9.7$ mm glass beads immersed in the RIM liquid L2.

The cell is illuminated from the back by a homogeneous white led panel and a high-speed camera (model FASTCAM SA-3 supplied by Photron) positioned at the front records each experiment within a frame of 620×1024 pixels in size (length×height), covering the entire cell and providing a resolution of about 3.8 pixels per mm. The acquisition frequency is either 125, 250 or 500 frames per second, depending on the experiment. By superimposing all the images of a sequence, Figure 3 shows an example of trajectories for particles of diameter around 1.2 mm inside a random packing of 9.7mm matt glass beads after

immersion in the RIM liquid L2.

Note that in the very first trials, the trajectories were recorded with two perpendicular cameras and reconstructed accurately in the 3D space. However, this protocol involved much data and, more importantly, sensitive trajectory reconstruction that was difficult to achieve automatically. As the statistical analyses carried out on this preliminary data proved to be completely similar in both x and y lateral directions, we decided to retain only one camera for our statistical study, providing solely $(x,\ z)$ trajectories by projection into the plane perpendicular to the camera axis

To this end, an automatic post-processing procedure was specifically developed to extract each individual trajectory using *ImageJ*. From the raw images captured by the camera, three regions of interest are first selected to separate the trajectories of particles L, M and R, then thresholded to obtain the vertical (z) and horizontal (x) position of each percolating particle at every time step t. From these position measurements $x(t)$ and $y(t)$, a smoothed derivation calculation based on a 10-point Savitzky-Golay filter provides the instantaneous velocities: u_x, u_z and the norm u [58]. This calculation also determines the upper boundary of the granular bed which is associated with a sudden decrease in particle velocity. The z-positions before penetration are used to evaluate the particle's settling velocity u_s by linear regression.

From a quantitative point of view, this trajectory tracking was carried out on a large number of particles to enable a comprehensive statistical analysis of submerged unimpeded percolation. Exactly 460 and 420 independent particle paths were recorded in liquid L1 and liquid L2 respectively, for the most part through random packs of 9.7 mm beads and in a minority of cases through a random pack of 7.3 mm beads.

III. EXPERIMENTAL PHENOMENOLOGY AND SOME UNEXPECTED OBSERVATIONS

A. Typical trajectories and percolation kinematics

An essential point to be emphasized beforehand is that the supposedly endless percolation motion of a particle can be definitively stopped by trapping within the porous medium, even when there are no constrictions in the bead pack small enough to completely obstruct the particle passage. As shown in the previous Fig. 3, 1.2 mm-particles L and M are more or less rapidly blocked inside the porous medium, despite the smallest constriction being 1.5 mm. This unexpected trapping will be examined in detail in the next section, serving as the primary focus of the present study.

Prior to this, let us take a closer examination of the particle kinematics along their path. To this end, two typical examples of trajectories followed during percolation in a packing of 9.7 mm beads are shown in Figure 4. Here, for the purpose of comparing the effects of different liquids, we have chosen percolating particles with exactly the same diameter, measured as $d = 1302\ \mu$m. The curves $x(t)$ and $z(t)$ in blue and red distinguish the trajectories in liquids L1 and L2, respectively. As explained earlier, the very first part of each particle trajectory corresponds to simple sedimentation in the liquid until penetrating the porous medium. The curves show indeed insignificant variation in x, while z increases linearly with time. A standard linear regression provides the corresponding settling velocity u_s as illustrated in Fig. 4 by the dashed lines in navy blue for liquid L1 and purple for liquid L2.

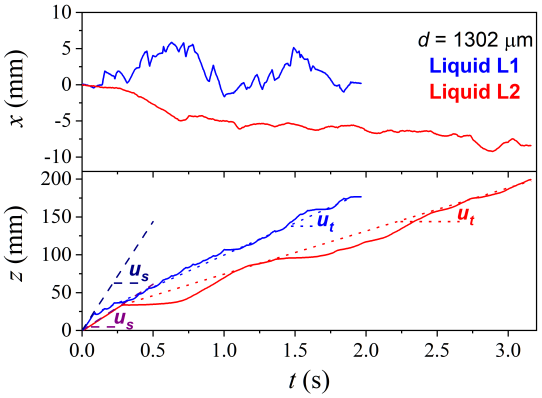

FIG. 4. Trajectories characterized by x and z positions over time for two particles of the same diameter $d = 1302\ \mu$m through a random pack of 9.7 mm glass beads in liquid L1 (blue curve) and liquid L2 (red curve). The dashed and dotted lines stand for steady settling and percolation paths in liquid L1 (in navy blue and blue) and liquid L2 (in purple and red).

Once inside the porous medium, the trajectory henceforth reflect percolation regime and appear quite different. Firstly, x-displacements are no longer negligible, corresponding to the lateral deviations required to move from one constriction to the next. However, overall lateral spreading remains very limited, rarely exceeding one or two coarse bead sizes along the complete percolating path. This observation justifies our strategy of releasing simultaneously three particles. It should also be noted that this is consistent with the "slither" percolation mode theoretically studied by Wilkinson and Edwards [30], for which a negligible lateral dispersion was calculated. Then, examining the evolution of z over time, the overall trend is still found to be roughly linear, even if there are significant deviations, with a substantially reduced slope compared to that during sedimentation. We can therefore conclude that a particle percolating through the bead pack progresses at an almost constant effective transit velocity, denoted u_t.

These observations are further highlighted by plotting the instantaneous vertical velocities u_z of the two particles in each liquid, as shown in Figure 5. The transit kinematics through the bead pack are characterized by an irregular and highly non-stationary evolution of the par-

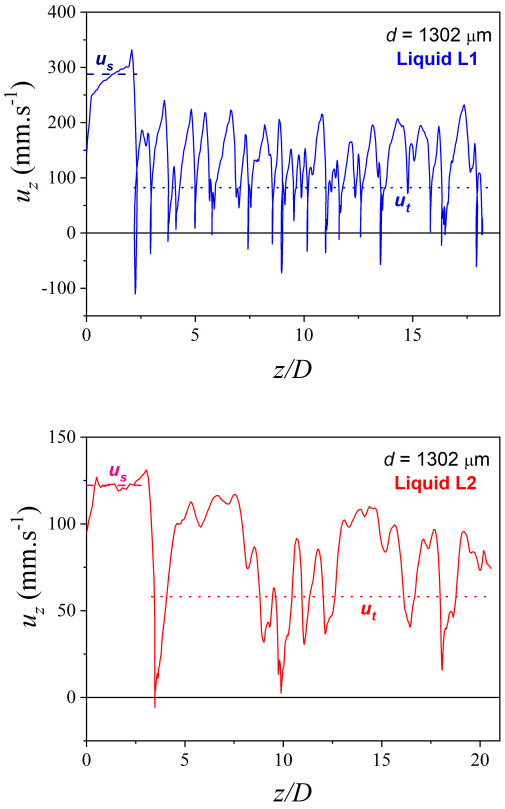

FIG. 5. Vertical velocity u_z calculated from the two trajectories of Fig. 4 as a function of the dimensionless depth z/D: (Top) in liquid L1; (Bottom) in liquid L2. The dashed and dotted lines show settling and transit velocity, in navy blue and blue in liquid L1 and in purple and red in liquid L2.

ticle's velocity with sudden decreases, possibly leading to transient halts, followed by phases of re-acceleration. In addition, there are some negative vertical velocity values for the percolation trajectory in liquid L1, corresponding to rebounds. However, these are no longer observed in liquid L2. This is perfectly consistent with the results of the coefficient of restitution for a particle in a liquid as already presented in Fig. 1, since the values of the Stokes number St of the two particles calculated from their settling velocity u_s are 125 in liquid L1 and only 5 in liquid L2, respectively above and below the critical value $\mathrm{St}_c \sim 10$. We can also notice that the maximal velocity approaches u_s, particularly in liquid L2 at lower Stokes number, although without reaching it completely. Figure 3 provides some complementary analysis of the trajectory shape, revealing the existence of a succession of elliptical-shaped sections, corresponding to a movement following the topology of the stack, where the percolating bead remains in contact with one, or even two, static coarse beads of the pack. Its velocity increases on these paths as the inclination steepens, until contact is lost, and then returns to simple sedimentation along a more vertical trajectory to the next contact.

Going a step further, a brief quantitative analysis of the percolation kinematics can be carried out. First, the effective transit velocity u_t is calculated for each mobile particle by the ratio between the distance traveled $\Delta z = z_f - z_i$ and the path duration $\Delta t = t_f - t_i$, where z_i and t_i refer to the position and moment at which the first deceleration is detected, defining the entry of the particle into the porous medium. The final position and time, z_f and t_f, coincide either with the arrival of the particle at the bottom of the bead pack, or with its definitive trapping within the porous medium at a position $z_f = z_{trap}$ and a corresponding depth equal to $\Delta z_{trap} = z_{trap} - z_i$. Note that u_t could also be calculated by linear regression of $z(t)$ or by averaging the vertical velocity u_z of the particle as it travels through the porous medium. However, the values obtained by the three alternative methods are quite similar and consistently differ by only a few percent. The u_t values obtained for the trajectories of Fig. 4 and Fig. 5 are represented by the two dotted lines in blue for liquid L1 and red for liquid L2.

From there, we performed statistical averages by classifying the released particles into size intervals. More precisely, by selecting a population of particles with diameters measured between d_m and d_M, we determine its mean diameter $\langle d \rangle_{[d_m,d_M]}$ and related standard deviation, as well as the corresponding mean settling and transit velocities, with their respective standard deviations, denoted in the following U_s and U_t, and calculated as $U_{s,t} = \langle u_{s,t} \rangle_{[d_m,d_M]}$. The results obtained for all the experiments carried out with zirconium particles are shown in Figure 6 with circular symbols for U_t in blue (liquid L1) and red (liquid L2), and triangular symbols for U_s in navy blue (liquid L1) and purple (liquid L2). As expected, there is a significant shift between U_s and U_t. The settling velocity U_s exhibits a very similar trend with particle size in both liquids.

To further investigate this initial sedimentation phase, the drag coefficient of the settling particles can be determined. Indeed, once terminal sedimentation velocity is reached, the balance between drag and buoyancy forces for a sphere gives the following relationship for the drag coefficient: $C_d(\mathrm{Re_p}) = \frac{4}{3}\mathrm{Ar}\mathrm{Re_p}^{-2}$ where $\mathrm{Re_p} = \rho_\mathrm{i} \mathrm{u_s} \mathrm{d}/\mu_\mathrm{i}$ and $\mathrm{Ar} = \rho_i(\rho_p - \rho_i)gd^3/\mu_i^2$ are the particle's Reynolds number and Archimedes number respectively, with $i \in \{1, 2\}$ referring to the liquid L_i being considered. As shown in the bottom graph of Fig. 6, the values obtained for the drag coefficients are perfectly consistent with one another and with the data of the literature, given the good agreement found with Dallavalle's empirical law [59, 60] which is valid for $\mathrm{Re_p} < 3000$, broadly encompassing the range of our experiments, and which is given by:

$$C_d = \left(\sqrt{24/\mathrm{Re_p}} + \sqrt{0.44}\right)^2. \qquad (2)$$

If we now analyze percolation itself through the mean transit velocity U_t in Fig. 6, we can first notice substantially higher standard deviations compared to U_s, which

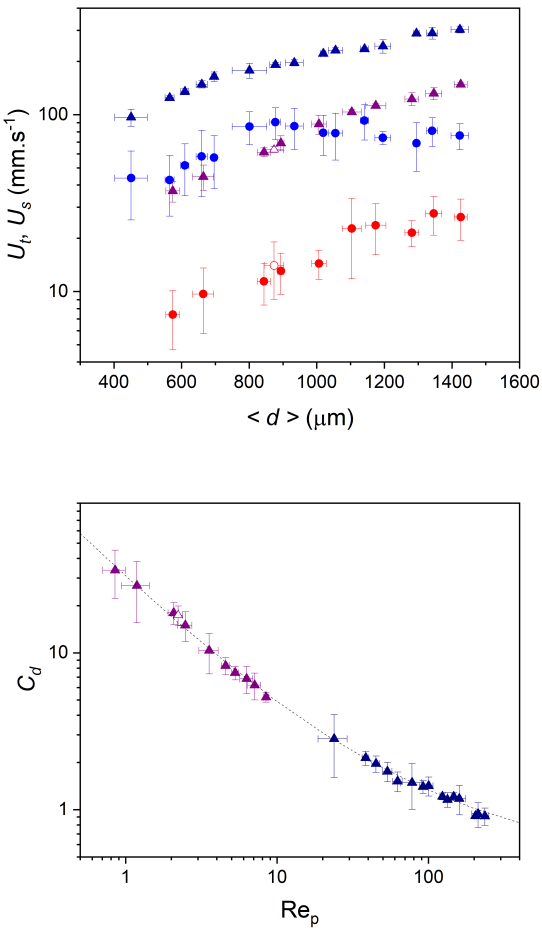

FIG. 6. (Top) Mean settling velocity U_s and mean transit velocity U_t as a function of mean particle diameter $\langle d \rangle$, after statistical particle size averaging. (Bottom) Drag coefficient C_d versus particle Reynolds number $\mathrm{Re_p}$ in the initial sedimentation phase before percolation with the dotted curve representing Dallavalle's empirical law given by Eq. (2) [59]. U_t is displayed by circular symbols in blue (liquid L1) and red (liquid L2). U_s and C_d are displayed by triangular symbols in navy blue (liquid L1) and purple (liquid L2). Almost all the data correspond to random packs of 9.7 mm beads (solid symbols), with the exception of one series produced in a pack of 7.3 mm beads (open symbols). Error bars represent standard deviations.

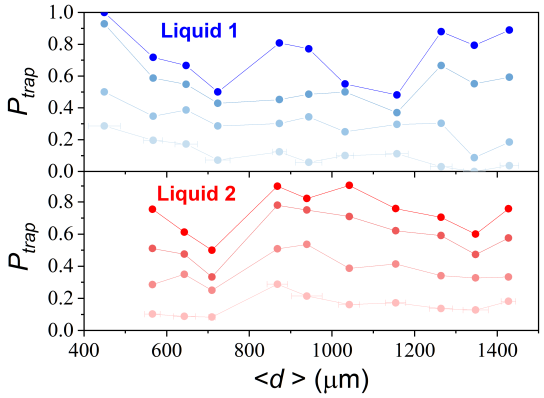

FIG. 7. Trapping probability as a function of the mean particle diameter $\langle d \rangle$, after statistical particle size averaging and for $D = 9.7$ mm. Data in blue for liquid L1 (top) and red for liquid L2 (bottom) correspond to a probability calculation based on approximately the total pack height ($H/D = 16$), while data with related shaded colors are obtained by considering decreasing depths ($H/D = 10$, 5 and 1) from the top of the packing.

underlines a far much more erratic behavior of the particles when moving through the porous medium, in contrast to their prior sedimentation fall. This variability in the transit velocity has two origins. One reflects the huge fluctuations of the instantaneous percolation velocity over time for a given particle, as highlighted by Fig. 5. The other stems from the inherent erratic nature of the trajectories, leading to a wide dispersion when averaged over a large number of individual paths. Furthermore, similarly to the settling velocity, a progressive increase of U_t with particle size is observed, except in the range of the largest diameters, particularly in liquid L1 where a saturation occurs, typically above 800 μm. The gap between mean transit velocities in the two liquids then narrows, but remains significant, with the ratio U_{t_1}/U_{t_2} decreasing from around 6 to just below 3. It is also interesting to note that, while settling velocities U_s are logically similar for the two tested sizes of beads in the pack (solid symbols for $D = 9.7$ mm, open symbols for $D = 7.3$ mm and in liquid L2), the same holds for the transit velocity U_t, at least in the particle size range considered here, around 900 μm. Contrary to what has been reported for dry percolation, this seems to indicate that the transit velocity under submerged conditions is no longer simply dependent on the size ratio $\delta = \langle d \rangle / D$.

After this overall description – first qualitative and then quantitative – of the percolation kinematics of spherical particles in a porous medium consisting of an immersed pack of beads, we now focus on one of the key observations made: the unexpected existence of particle entrapment even though the packing geometry is geometrically open to their passage and would, in principle, allow for unlimited percolation paths.

B. Particle trapping and metastability

To conduct a systematic study of trapping in the porous medium, a first step is to assess the probability of trapping as a function of particle diameter. Based on a similar statistical averaging, the overall trapping probability P_{trap} is calculated for each particle size class as the ratio of the number of deposited particles to the total number of releases. The data are shown in Figure 7. Firstly, regardless of size, the probability that

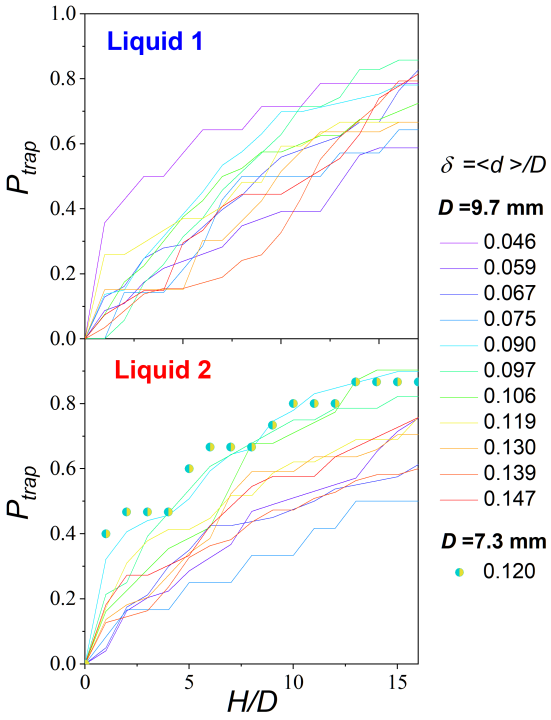

FIG. 8. Cumulative trapping probability when increasing the depth ratio H/D under consideration, in liquid L1 (top) and liquid L2 (bottom), for several size ratios δ in packing of spheres with $D = 9.7$ mm (colored lines) and only one value of δ with $D = 7.3$ mm (bi-color symbols referring to the mobile particle in the 9.7 mm bead pack with either the same diameter of 880 μm, in cyan, or the same size ratio $\delta = 0.12$, in yellow).

a particle transiting through the bead pack will be definitely stopped is very high, between 50% and 100% when considering the entire height of the pack. The same calculation can also be carried out for a smaller depth H from the upper surface, and the corresponding values have been added to Fig. 7, from top to bottom, for $H/D = 10$, 5 and 1, in shades of blue and red for liquid L1 and liquid L2, respectively. As expected, these probabilities progressively grow with the depth of exploration. If a significant fraction of the particles are blocked at the very first layer, the increase in probability with H then appears fairly regular as also displayed on the cumulative trapping probability in Figure 8.

In addition, and this is the second key observation from Fig. 7, we can note that some particle sizes are more likely trapped than others. This effect is amplified with increasing height, making it possible to identify specific size ranges of reduced trapping probability accross the entire porous medium: around 700 μm for both liquids, in the 1000-1200 μm range for liquid L1 and around 1350 μm for liquid L2.

We performed only one series of particle releases through spheres of diameter $D = 7.3$ mm and these data have been plotted in Fig. 8, corresponding to particles with a mean diameter $\langle d \rangle \approx 880$ μm and a mean size ratio $\delta \approx 0.120$. It is therefore natural to compare these data with the previous ones, obtained for $D = 9.7$ mm, either for the same diameter or for the same size ratio. As can be seen from the graph, the best agreement is achieved when the diameters are equal, suggesting that this parameter is more relevant than size ratio in describing entrapment, consistent with what has already been observed earlier for the mean transit velocity.

A further consideration concerns the spatial distribution of trapped particles, and more specifically their depth, which can be inferred from the local slope of the curves in Figure 8. Excluding the first layer, these slopes are comparable, suggesting an approximately uniform distribution of trappping locations throughout the packing, except maybe for the largest particles in liquid L1. However, more statistics would be needed to confirm this observation. In addition, the first layer exhibits a distinctive behavior. Compared to the rest of the porous medium, it includes the top surface of the packing, which has two specific features with antagonistic effects on trapping. On the one hand, as will be discussed in the next section, the top surface offers a larger area where the local slope is low enough for a particle to be stopped. On the other hand, the particles arrive at this layer at their terminal settling velocity, which is somewhat higher than the velocities subsequently reached in the medium (see Fig. 5), thereby increasing the possibility of multiple rebounds. However, this latter argument only applies to liquid L1 with large enough particles, since in all other cases the coefficient of restitution is either low or virtually null, as already illustrated in Fig. 1. Indeed, we observe in liquid L1 that the peak of the first layer decreases when the diameter of the particles increases and almost disappears for $\delta \approx 0.14$, when the coefficient of restitution becomes significant. This is also apparent in the curve corresponding to $H/D = 1$ in Fig. 7. The trend is more difficult to identify in liquid L2, where bounces no longer occur. However, a decrease in trapping in the first layer is observed for the smallest particle sizes (also visible for $H/D = 1$ in Fig. 7), although there is no clear explanation for this.

Another notable aspect of this unexpected particle trapping phenomenon concerns its stability. More specifically, we investigated whether a weak mechanical stress, generated by gentle shaking, could restore motion to the trapped particles. For this purpose, we used the mass release protocol presented in Sec. II B to generate a large number of trapping events. This approach involves collective effects between intruding particles, but enables better statistical analysis and direct visualization of mechanical particle remobilization. For these experiments,

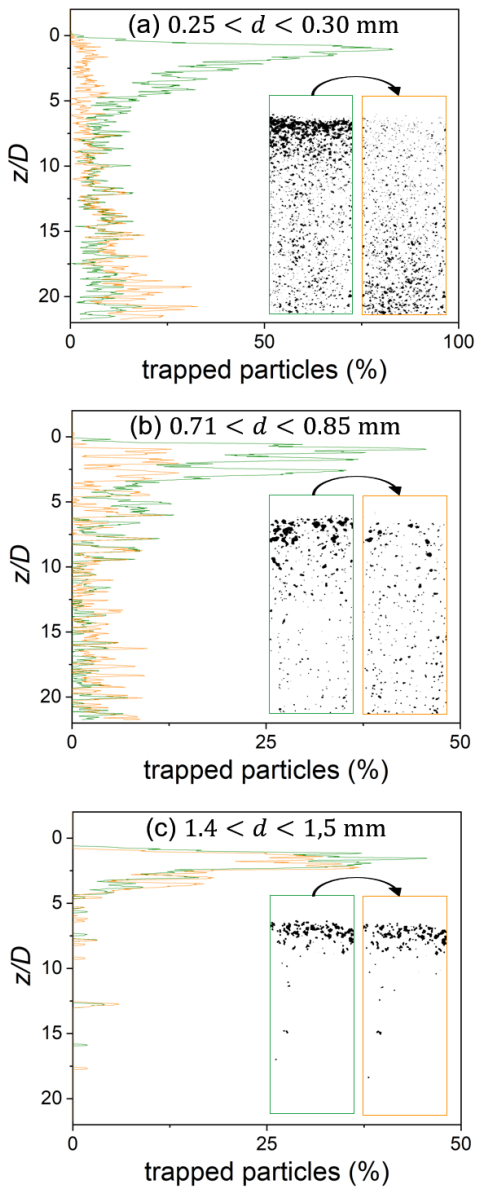

FIG. 9. Vertical profiles of trapped particle concentration (in %) inside a 7.3 mm bead pack immersed in liquid L2 before (green) and after (orange) gentle shaking for painted glass particles of diameter: (a) 250 μm $< d <$ 300 μm; (b) 710 μm $< d <$ 850 μm; (c) 1400 μm $< d <$ 1500 μm. Insets: Corresponding thresholded image after background subtraction.

the granular sample is made up of glass beads of 7.3 mm diameter immersed in liquid L2. For stock availability, we used here a different set of injected particles, namely painted glass beads (Decobeads) in the following three size ranges: 0.25 mm $< d <$ 0.3 mm, 0.71 mm $< d <$ 0.85 mm, and 1.4 mm $< d <$ 1.5 mm. The images in the insets of Figure 9, obtained after background subtraction and thresholding, correspond to the initial particle trapping and then the new equilibrium position obtained following a gentle shaking sequence. In practice, a Casagrande cup [61] is placed on a plate, positioned at the top of the cell, and used to reproducibly generate a sequence of 100 low-amplitude shocks. The images first show significant initial trapping and progressively deeper penetration as particle size decreases. More strikingly, the effect of shaking varies greatly according to particle size. The largest particles remain trapped, while the finest are massively remobilized and subsequently recaptured further away. In Fig. 9, trapped particle concentration profiles, obtained by integrating grey levels over each horizontal line of the previous inset binary images, illustrate this effect by comparing before-shaking (green) and after-shaking (orange) profiles. In conclusion, while trapping appears robust for large particles, it is inherently metastable for small particles, since low levels of mechanical energy can destabilize the local equilibrium at the trapping site.

IV. ANALYSIS OF TRANSIT VELOCITY AND PARTICLE TRAPPING

This section presents specific arguments and complementary experiments aimed at qualitatively revealing the physical mechanisms behind particle trapping in a geometrically open granular pack immersed in a viscous liquid, as previously evidenced.

A. Key role of viscous drag and lubrication

In contrast to the previous literature on dry percolation [24, 28–30, 32, 35, 40], it is obvious that the presence of the interstitial liquid is a necessary condition for particle trapping, since the latter is virtually not observed in air. During dry percolation, the motion of a particle in a grain packing is purely ballistic, consisting of bounces and portions of parabolic trajectories. The typical transit velocity U_t scales with the average ballistic velocity between 2 rebounds, that is, $\sqrt{gD}$. Compared to this characteristic percolation velocity in air, which is around 0.3 m.s^{-1} in the present study, we note in Fig. 6 that the transit velocities in both liquids are up to more than an order of magnitude lower.

Indeed, the surrounding liquid has a dual effect. On the one hand, it significantly reduces particle velocity due to viscous drag, and on the other hand, it substantially enhances dissipation during rebounds by lubrication. As already mentioned, if the Stokes number falls below a threshold of about 10, for instance due to high liquid viscosity and/or small particle size, dissipation becomes so strong that no rebound occurs at all [43]. This is precisely the case in all our experiments with liquid L2 (see Fig. 1).

As suggested by the fact that the terminal settling velocity U_s is reached during the falling phase in the pure liquid before entering the granular medium, the drag force can progressively dominate over inertia. So the mo-

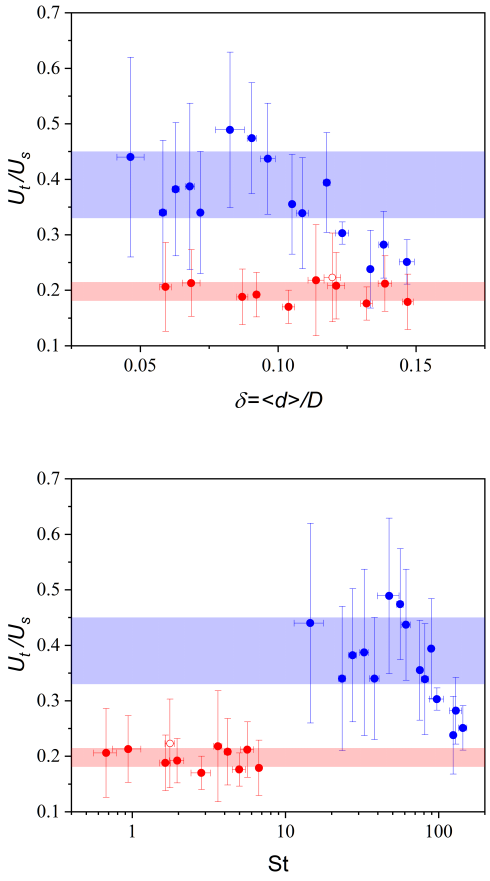

FIG. 10. Data from Fig. 6 plotted in dimensionless form by representing U_t/U_s as a function of (top) the size ratio δ and (bottom) the Stokes number St (calculated with the settling velocity U_s) in liquid L1 (blue symbols) and liquid L2 (red symbols).

tion of a particle in the pore space consists of a succession of transient settling stages that tend to U_s as illustrated in Fig. 5. Accordingly, the mean transit velocity U_t is therefore expected to scale with the settling velocity U_s.

To assess this scaling, Figure 10 shows the ratio U_t/U_s as a function of either the size ratio δ or the Stokes number St. From this graph, we observe that, throughout most of the range explored, typically for St<80, the ratio U_t/U_s remains relatively constant for a given liquid, with only minor dispersion, and stays below 1 as expected. It may be noted incidentally that, even though the hydrodynamic regimes of particle migration are very different, these velocity ratios fall within the typical range between 0.1 and 0.5 obtained for $U_t/\sqrt{gD}$ in the case of dry percolation [28–30, 32, 35, 40]. However, two striking points raise questions. First, there is a noticeable decrease in U_t/U_s for the largest particles in liquid L1. Second, the data obtained with the two liquids do not collapse onto a single trend.

As shown in Fig. 10b, the decrease in U_t/U_s in liquid L1 occurs at high stokes number and likely indicates a transition to a visco-ballistic regime where lubricated rebounds play an increasingly prominent role. Consequently, the trajectories should be significantly more tortuous than in the absence of rebounds. This is clearly demonstrated in Figure 11, which shows the mean tortuosity [62]. of the trajectories as a function of the Stokes number. Below a threshold St∼80, tortuosity changes little regardless of the liquid, remaining slightly above 1. In contrast, above this threshold, there is a sharp increase, indicating much more erratic trajectories resulting from bouncing.

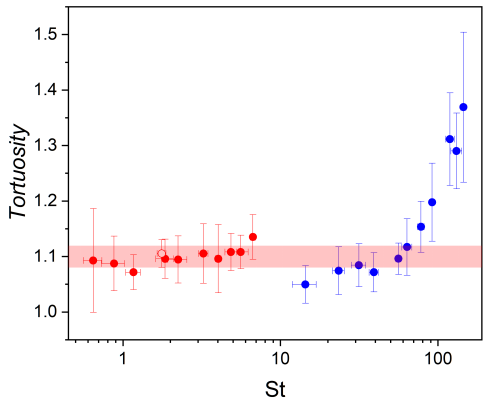

FIG. 11. Mean trajectory tortuosity as a function of the Stokes number St (calculated with the settling velocity U_s) in liquid L1 (blue symbols) and liquid L2 (red symbols).

Although Fig. 10b shows, for Stokes numbers typically below 80, the relevance of the terminal settling velocity as the characteristic transit velocity in the porous medium, the quantitative difference in U_t/U_s between the liquids remains significant, being approximately 0.4 in liquid L1 and 0.2 in liquid L2. This discrepancy occurs even though the corresponding trajectories exhibit similar tortuosity. The proposed scaling is therefore only partially satisfactory as obviously the settling velocity does not fully capture all aspects of transit dynamics. It is likely that another velocity comes into play, not during the settling phases but when the particle progresses while in contact with the porous matrix. Indeed, highly damped or even virtually nonexistent rebounds lead to prolonged contacts between the moving particle and the solid obstacles formed by the spheres in the packing. As already described in Sec. III A, the trajectory then follows the surface of the contacted sphere, with a small velocity amplitude proportional to the local slope. Furthermore, the particle may frequently come into contact with a second sphere, effectively doubling the lubrication force and further reducing its velocity. On average, the transit time of a particle along its path is substantially increased by the single- or double-contact segments with the static beads of the granular pack. As a result, its

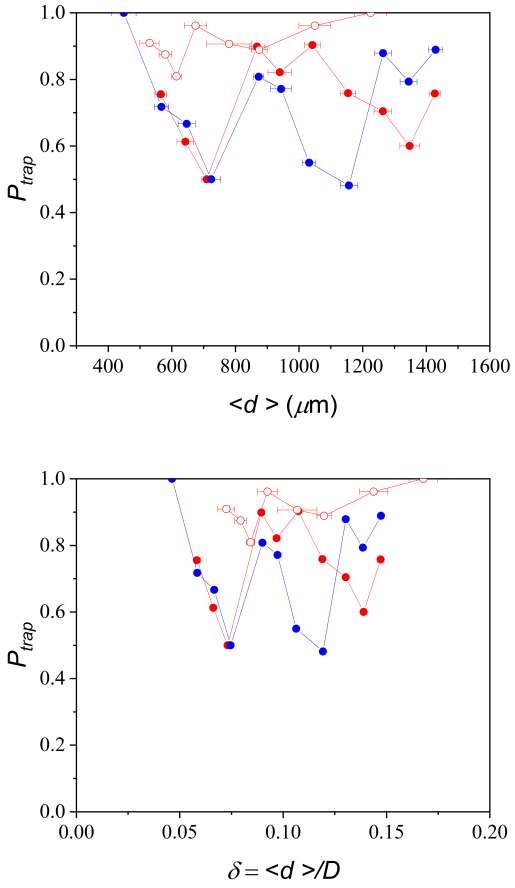

FIG. 12. Trapping probability as a function of (top) the mean particle diameter $\langle d \rangle$ and (bottom) of the mean size ratio δ, in liquid L1 (blue symbols) and in liquid L2 (red symbols) over a pack height $H/D \approx 16$ with beads of diameter $D = 9.7$ mm (closed symbols) and $D = 7.3$ mm (open symbols).

mean transit velocity decreases accordingly. We will return to this characteristic "in-contact" velocity later.

Regarding the trapping mechanism highlighted in this study, combined low-slope and double-contact situations, where particle velocity is very low, definitely offer opportunities for blocking a particle as soon as solid contact is established with adjacent static beads, that is, when solid friction is activated. Nonetheless, as shown in Figure 12 which reproduces the trapping probabilities over the total height of the pack from Fig. 7 but for two different coarse bead sizes, the trapping efficiency in liquid L1, where the viscous damping is much less pronounced, remains quantitatively very similar to the bounce-free case in liquid L2. More specifically, we find almost identical values of trapping frequency for the smallest particles, followed by much more significant differences for particles larger than 1 mm, i.e. $\delta > 0.1$. Interestingly, this threshold nearly coincides with the aforementioned reduction of U_t/U_s in liquid L1, typically for Stokes numbers St beyond 80 (see Fig. 10). However, the trapping data cannot be quantitatively reproduced when performing similar experiments (as those described in Sec. IV B) in liquid L2, using the same fine particles – and hence the same low Stokes numbers – but with a granular packing of smaller beads ($D = 7.3$ mm). The qualitative W-shape curve remains reasonably similar, but no consistent scaling is observed for either the trapping probability or the x-axis variable, whether particle diameter or size ratio is considered. In the end, even if there is no major quantitative difference when varying the viscosity value between L1 and L2, the presence of a viscous surrounding liquid remains essential for trapping, as no equivalent is observed in dry conditions. This also suggests that the decisive contribution to trapping must come from solid friction, whose critical role will be discussed in the next section.

However, before doing so, it should be noted that everything discussed above about the contribution of viscosity to trapping relates only to the particular situation studied here, where the surrounding liquid is at rest. Conversely, in previous filtration experiments carried out under controlled interstitial flow, unimpeded percolation has been exclusively reported under conditions where the filtering granular bed is geometrically open, without any particle entrapment [1, 44, 45]. In this specific situation, the characteristic transit velocity of the mobile particles would therefore be chosen equal to the mean velocity of the interstitial flow (instead of the settling velocity), as recently confirmed by results obtained from coupled DEM-PFV numerical simulations [37].

B. Key role of friction

To demonstrate the role of friction in the previously identified trapping mechanism, experiments were carried out using the same batch of fine particles but beads of the porous matrix with different surface properties. More specifically, we successively used the matt and polished glass beads already described in Sec. II A, as well as hydrogel beads (supplied by Aquabeads). The surface finish thus ranges from rough to smooth, and even to extremely smooth and slippery for the hydrogel beads, which can be considered virtually frictionless, with a coefficient of friction about $0.02 - 0.03$ [63, 64]. Regarding optical matching, the series of experiments with matt and polished glass beads was conducted only with our most viscous liquid L2 (see Sec. II A). As for the hydrogel beads, they are composed of hydrophilic polymers that swell considerably when immersed in an aqueous solution. They absorb several times their volume of liquid, becoming very soft and reaching a refractive index almost equal to that of the surrounding liquid. Here, a water-glycerol mixture was chosen with a viscosity comparable to that of liquid L2. In all three cases, the beads are spherical and of nearly identical size – 10 mm for the glass beads and about 11 mm for the hydrogel beads after swelling. All samples are comparably disordered, with similar volume

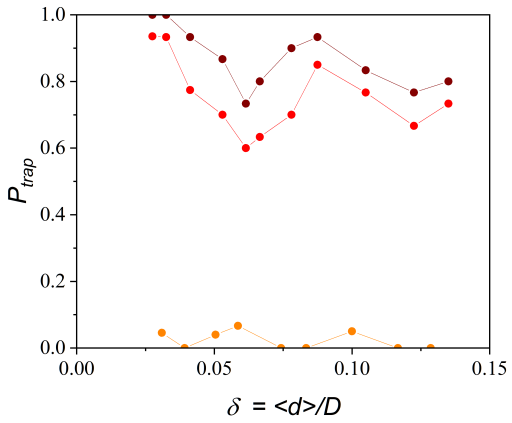

FIG. 13. Trapping probability as a function of the mean size ratio $\delta = \langle d \rangle / D$ in polished (red symbols) and matt (dark red symbols) glass beads of diameter 10 mm, and hydrogel beads (orange symbols) of diameter around 11 mm, with immersion liquids equal to L2 or of comparable viscosity.

fraction (around 0.62) and a total height of about 17 cm. Thus, the three porous matrices are virtually identical, differing only in the solid friction at the bead surface.

Extending the range of porous configurations investigated while ensuring statistically robust trapping data led us to streamline the experimental protocol: trajectory tracking was omitted, and attention was restricted to determining whether the small beads were trapped or percolated through the medium. Subsequently, from individual releases of the same zirconium beads, the trapping probability as a function of the mean size ratio δ was determined for each of the three granular packs, as shown in Figure 13. Each probability value was calculated from 30 identical particle releases, amounting to a total of approximately 1,000 releases for all data presented. Compared with the previous case using polished glass beads (red symbols), a noticeable increase in the number of trapped particles is observed with the rougher matt beads (dark red symbols). Interestingly, the increase in the probability of trapping induced by surface roughness is relatively uniform, about 10% regardless of the size of the mobile particles. Consistently, we identify approximately the same size ranges as in Sec. III B, where trapping efficiency is slightly lower, around 600 and 1200 μm. Most importantly, the results of Fig. 13 show an almost complete disappearance of particle trapping with the hydrogel beads (orange symbols), i.e. in the absence of friction. This provides conclusive evidence for the essential role of friction in the trapping mechanism identified in this study which, together with the conclusions of Sec. IV A, can be named as *visco-frictional trapping*.

Focusing specifically on the potential trapping of a particle in the immediate vicinity of a sphere from the granular medium, the hydrogel bead provides an experimental illustration of the "slither" percolation mode conceptualized by Wilkinson and Edwards [30], as already mentioned above: the particle simply slides over a thin lubricating liquid layer, without any direct solid–solid contact. By contrast, in the two other cases (matt and polished glass beads), frictional contact is activated, causing the particle to roll over the static sphere. As in the usual dry contact situation, this rolling is combined with sliding once the local slope exceeds a threshold. This description is consistent, for example, with the model proposed by Smart and Leighton [65] for the motion of a sphere along an inclined plane, which accounts for both hydrodynamic forces and solid friction, under the assumption that particle roughness determines the lubrication gap between the two solid surfaces. Experimental measurements have validated this model, mainly for artificially roughened particles [65–69]. It should be noted that this type of artificial roughness has also been shown to influence normal rebound on the surface [65, 66, 70]. Alternatively, Jenkins and Koenders [71] proposed a model in which particle roughness is represented by a realistic porous shell, leading to even stronger hydrodynamic interaction forces when the particle approaches the plane perpendicularly. These models deal with the lubricated contact between a sphere and a plane, while the present situation involves a moving sphere interacting with one or two larger, fixed spheres. It is nevertheless likely that the qualitative behavior remains very similar.

At low Reynolds numbers, the Smart and Leighton model [65] predicts that, for a sphere in lubricated contact with an inclined plane, the tangential velocity is directly proportional to the local slope, and represents only a small fraction of the particle's settling velocity, i.e. the so-called Stokes velocity, $U_{St} = \frac{(\rho_p - \rho_l) g d^2}{18 \mu_l}$. The relatively low Reynolds numbers in our experiments – typically Re < 10 during the contact phase in liquid L2 and for the smallest mobile particles in liquid L1 – suggest that Stokes velocity can serve as a reference velocity when the particle transits in contact with the porous matrix. It is thus consistent to test an alternative scaling to that of the previous section IV A, by normalizing the mean transit velocity U_t with the Stokes velocity U_{St}, as shown in Figure 14. Despite some dispersion, a better collapse of data is found from the two liquids, at least in the expected range for St$<$80 where bouncing has a negligible effect. Although the scaling is not fully satisfactory, it provides a consistent framework for understanding particle transit as a complex process involving two characteristic velocities: the terminal settling velocity during free-falling portions, and a visco-frictional velocity, close to the Stokes velocity, during phases of circumvention of the packing spheres.

Finally, to further understand the local trapping process, we need to take into account the spherical shape of the percolating particles. Sliding friction allows a particle to roll on contact with a solid surface, but cannot stop it. Rolling friction, by contrast, is the only mechanism capable of bringing the particle to a complete halt, which

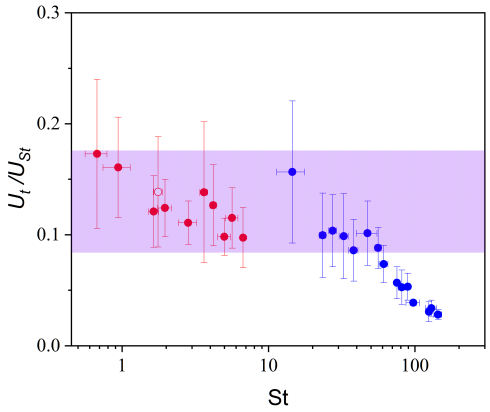

FIG. 14. Data from Fig. 6 plotted in dimensionless form by representing U_t/U_{St}, with U_{St} the Stokes velocity, as a function of the Stokes number St (calculated with the settling velocity U_s) in liquid L1 (blue symbols) and liquid L2 (red symbols).

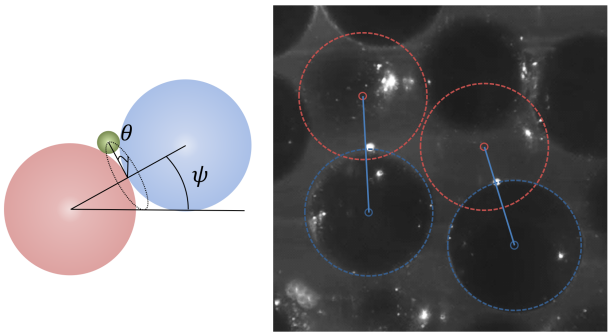

FIG. 15. (Left) Definition of the angles ψ and θ, which specify the position of the trapped particle (in green). (Right) Image showing two trapping sites for zirconium particles of approximately 400 μm in diameter within a packing of 10 mm polished glass beads immersed in liquid L2. The trapped particles appear in white. The upper trapping beads are highlighted by blue circles in the laser plane, while the lower ones are marked by red circles following a similar identification in a slightly deeper plane.

becomes realistic at very low local inclinations, i.e. below the rolling resistance threshold. Double contacts further slow particle motion through increased lubrication while providing greater resistance to rolling and stabilizing the particle transversely. We thus conclude that trapping is most likely to occur when a particle comes into contact with two beads at low inclination. This physical interpretation is supported by a limited number of direct observations within the translucent porous medium as illustrated in Figure 15. In practice, a horizontal laser sheet was translated vertically to locate the trapping sites and characterize their local geometric arrangement from a top-down view. Fig. 15(right) corresponds to a laser plane located approximately at the equatorial plane of the two upper coarse beads. Two small particles can be seen to be trapped within this plane. Such an equilibrium configuration is only possible due to an additional contact with a second coarse bead located deeper in the packing, whose position was identified through the vertical scanning of the laser sheet. This scan allows reconstruction of the trapping-site geometry, as illustrated in Fig. 15(left) where two local angles can be defined: ψ, the inclination between the centers of the two trapping balls relative to the horizontal, and θ, the orientation of the trapped particle's position relative to the vertical. In all measurements, two-contact trapping was systematically observed and, as shown in the examples in Fig. 15, all trapping sites exhibit very small values of θ, consistent with locally low inclinations.

C. Further influences on trapping

Lastly, a series of additional experiments have revealed several other parameters that influence trapping, although no systematic investigation has yet been conducted.

Since trapping is associated with locations where the mobile particle can simultaneously contact two beads of the porous matrix under low local inclination, the packing structure is expected to play a major role. In the case of random packings, as used in all previous experiments, the geometry remains statistically equivalent between trials, and only a dependence on the solid fraction ϕ could arise. This effect has not been explored here, all the more since ϕ cannot vary significantly in a packing of monodisperse spheres. However, the influence of the packing structure can be clearly demonstrated using ordered arrays. As described in Sec. II A, two nearly crystalline configurations were specifically constructed: one composed of 10 mm beads in a centered cubic (CC) arrangement, and another with 16 mm beads in a face-centered cubic (FCC) arrangement. The corresponding trapping probabilities measured in these ordered systems are shown in Figure 16 and compared with the previous results, all tests being performed with polished glass beads immersed in liquid L2.

It can be seen that, compared with the disordered case, the CC structure slightly reduces trapping efficiency, particularly for certain particle sizes, accentuating the dips in the W-shaped curve and noticeably shifting the dip at larger sizes. This effect is likely due to the existence of preferential pathways between the vertically aligned bead columns, along which percolating particles avoid any double-contact motion at low inclination.

In contrast, the FCC packing exhibits a strikingly different behavior: 100% of the particles released above the pile are trapped within the medium, even though its height, expressed in bead layers (H/D), is smaller. This implies that trapping systematically occurs within the very first layers, involving particles whose trajectories include several locations of almost zero local inclina-

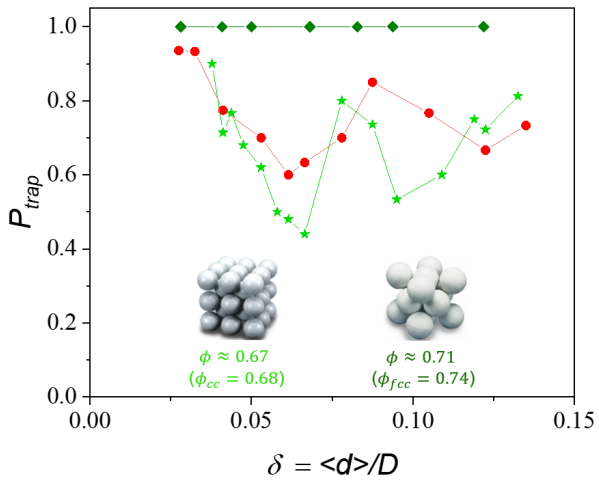

FIG. 16. Trapping probability as a function of the mean size ratio $\delta = \langle d \rangle / D$ in a random pack of 10 mm glass beads (red symbols), in a centered cubic (CC) arrangement of 10 mm glass beads (light green symbols), and in a face-centered cubic arrangement of 16 mm glass beads (dark green symbols), with immersion liquid L2.

tion. Furthermore, with a coordination number of 12, the FCC structure inherently provides more contact points between beads than the CC structure, where the coordination number is only 8.

Overall, although geometric effects are most pronounced in ordered packings, they remain relevant for any internal structure, as they control both the number of sites suitable for trapping and the accessibility of these sites to mobile particles.

Finally, the shape and size of the mobile particles also exert a substantial influence on their trapping. As shown in the preceding results, the trapping probability is never uniform for particles in the percolation regime, but clearly depends on their diameter. This dependence, however, is intricate, exhibiting a non-monotonic evolution with peaks and valleys – previously referred to as W-shaped curve – such that specific sizes display a greater propensity to penetrate the packing. At this stage, the underlying mechanisms of visco-frictional trapping are not yet fully understood, and further investigation of the elementary processes is required to explain this complex behavior. With regard to particle shape, it is more straightforward: deviating from the case of spherical grains hinders – or even prevents – the rotation of the particle at the contact point, thereby mechanically increasing the likelihood of visco-frictional trapping. Indeed, for 1 mm particles of nearly the same density, we measured that replacing painted glass beads (Sec. III B) with rounded sand grains increased the trapping probability in a 12 cm packing of 10 mm polished glass beads from 72% to 100%. This clearly demonstrates that shape plays a major role, even though a more systematic analysis of this effect remains to be conducted.

V. CONCLUSION AND OUTSTANDING ISSUES

In this study, we have identified a novel visco-frictional trapping mechanism affecting particle percolation through a submerged granular medium. This mechanism plays a crucial role when the interstitial liquid is at rest and particularly in the absence of geometric obstruction, i.e. when the percolating particles are small enough to pass through the narrowest constrictions of the porous medium. Combining refractive index matching with high-speed imaging, our experimental set-up enabled detailed observation and analysis of particle trajectories and kinematics. The core finding is that trapping results from a critical interplay between viscous lubrication and solid friction, primarily occurring in situations involving double-contact and low local slope within the packing structure.

Particle transit prior to trapping can be understood as a complex process involving two characteristic velocities: the terminal settling velocity during free-falling portions, and a slower visco-frictional velocity during phases where the particle moves in single or double contact with the packing spheres. This dual-velocity framework captures the essence of the visco-frictional transit and its dependence on both hydrodynamic and solid-contact effects.

We found that the trapping mechanism is metastable, with particles capable of being remobilized under weak mechanical stress. Trapping probability depends on the particle size, the interstitial liquid viscosity, and the structure of the granular packing, with certain size ratios and ordered arrangements exhibiting distinct trapping behaviors. Additionally, surface properties of the granular pack, particularly friction, were shown to be critical, as evidenced by the near absence of entrapment in frictionless hydrogel beads.

While this study successfully elucidates the fundamental physics of visco-frictional trapping, it also opens avenues for future research. In particular, the observed, and perhaps most puzzling, W-shaped dependence of trapping probability on particle size remains an intriguing open question, suggesting subtle geometric and hydrodynamic effects yet to be fully uncovered. Further investigation into the roles of grain shape and packing heterogeneity is also warranted.

These findings bear significant implications for a wide range of applications, including filtration processes, sediment transport, and pollutant migration in submerged soils. A deeper understanding of visco-frictional trapping could help improve predictive models for sedimentary transport and enhance strategies for contaminant remediation in porous environments.

DATA AVAILABILITY STATEMENT

The data reported in this study are openly available [72].

[1] C. Ghidaglia, L. de Arcangelis, J. Hinch, and E. Guazzelli, "Transition in particle capture in deep bed filtration," *Physical Review E*, vol. 53, pp. R3028–R3031, 1996.

[2] G. Crini and E. Lichtfouse, "Advantages and disadvantages of techniques used for wastewater treatment," *Environmental Chemistry Letters*, vol. 17, no. 1, pp. 145–155, 2019.

[3] S. A. Bradford, J. Simunek, M. Bettahar, M. T. van Genuchten, and S. R. Yates, "Modeling colloid attachment, straining, and exclusion in saturated porous media," *Environmental Science & Technology*, vol. 37, no. 10, pp. 2242–2250, 2003.

[4] S. Song, P. Le-Clech, and Y. Shen, "Microscale fluid and particle dynamics in filtration processes in water treatment: A review," *Water Research*, vol. 233, p. 119746, 2023.

[5] J. E. Altoé F., P. Bedrikovetsky, A. G. Siqueira, A. L. S. de Souza, and F. S. Shecaira, "Correction of basic equations for deep bed filtration with dispersion," *Journal of Petroleum Science and Engineering*, vol. 51, no. 1, pp. 68–84, 2006.

[6] Y. Liu, H. Lu, Y. Li, H. Xu, Z. Pan, P. Dai, H. Wang, and Q. Yang, "A review of treatment technologies for produced water in offshore oil and gas fields," *Science of The Total Environment*, vol. 775, p. 145485, 2021.

[7] O. S. Alimi, J. F. Budarz, L. M. Hernandez, and N. Tufenkji, "Microplastics and nanoplastics in aquatic environments: Aggregation, deposition, and enhanced contaminant transport," *Environmental Science & Technology*, vol. 52, no. 4, pp. 1704–1724, 2018.

[8] K. Waldschläger and H. Schüttrumpf, "Infiltration behavior of microplastic particles with different densities, sizes, and shapes—from glass spheres to natural sediments," *Environmental Science & Technology*, vol. 54, no. 15, pp. 9366–9373, 2020.

[9] L. E. Frostick, P. M. Lucas, and I. Reid, "The infiltration of fine matrices into coarse-grained alluvial sediments and its implications for stratigraphical interpretation," *Journal of the Geological Society*, vol. 141, no. NOV, pp. 955–965, 1984.

[10] M. Brunke, "Colmation and depth filtration within streambeds: Retention of particles in hyporheic interstices," *International Review of Hydrobiology*, vol. 84, no. 2, pp. 99–117, 1999.

[11] S. Gibson, D. Abraham, R. Heath, and D. Schoellhamer, "Vertical gradational variability of fines deposited in a gravel framework," *Sedimentology*, vol. 56, no. 3, pp. 661–676, 2009.

[12] G. Gerber, S. Rodts, P. Aimedieu, P. Faure, and P. Coussot, "Particle-size-exclusion clogging regimes in porous media," *Physical Review Letters*, vol. 120, p. 148001, 2018.

[13] R. Dubuis and G. De Cesare, "The clogging of riverbeds: A review of the physical processes," *Earth-Science Reviews*, vol. 239, p. 104374, 2023.

[14] D. Marot and A. Benamar, "Suffusion, transport and filtration of fine particles in granular soil," in *Erosion of geomaterials*, pp. 39–79, 2012.

[15] S. Bonelli, ed., *Erosion in Geomechanics Applied to Dams and Levees*. ISTE Ltd and John Wiley Sons Inc, 2013.

[16] R. Kretzschmar, "Colloid-facilitated sorption and tranport," in *Encyclopedia of Soils in the Environment* (D. Hillel, ed.), pp. 276–284, Oxford: Elsevier, 2005.

[17] G. Wharton, S. H. Mohajeri, and M. Righetti, "The pernicious problem of streambed colmation: A multidisciplinary reflection on the mechanisms, causes, impacts, and management challenges," *WIREs Water*, vol. 4, no. 5, p. e1231, 2017.

[18] S. Sadeghnejad, F. Enzmann, and M. Kersten, "Numerical simulation of particle retention mechanisms at the sub-pore scale," *Transport in Porous Media*, vol. 145, p. 127–151, 2022.

[19] S. Gibson, D. Abraham, R. Heath, and D. Schoellhamer, "Bridging process threshold for sediment infiltrating into a coarse substrate," *Journal of Geotechnical and Geoenvironmental Engineering*, vol. 136, no. 2, pp. 402–406, 2010.

[20] N. Reboul, E. Vincens, and B. Cambou, "A computational procedure to assess the distribution of constriction sizes for an assembly of spheres," *Computer and Geotechnics*, vol. 37, no. 1-2, pp. 195–206, 2010.

[21] E. Vincens, K. J. Witt, and U. Homberg, "Approaches to determine the constriction size distribution for understanding filtration phenomena in granular materials," *Acta Geotechnica*, vol. 10, no. 3, pp. 291–303, 2015.

[22] T. Shire and C. O'Sullivan, "Constriction size distributions of granular filters: A numerical study," *Géotechnique*, vol. 66, no. 10, pp. 826–839, 2016.

[23] F. Seblany, E. Vincens, and C. Picault, "Determination of the opening size of granular filters," *International Journal for Numerical and Analytical Methods in Geomechanics*, vol. 45, no. 9, pp. 1195–1211, 2021.

[24] I. Ippolito, L. Samson, S. Bourlès, and J.-P. Hulin, "Diffusion of a single particle in a 3D random packing of spheres," *The European Physical Journal E*, vol. 3, pp. 227–236, 2000.

[25] R. Sakthivadivel and H. A. Einstein, "Clogging of porous column of spheres by sediment," *Journal of the Hydraulics Division*, vol. 96, no. 2, pp. 461–472, 1970.

[26] M. M. Roozbahani, L. Graham-Brady, and J. D. Frost, "Mechanical trapping of fine particles in a medium of mono-sized randomly packed spheres," *International Journal for Numerical and Analytical Methods in Geomechanics*, vol. 38, no. 17, pp. 1776–1791, 2014.

[27] A. Kerimov, G. Mavko, T. Mukerji, and M. A. Al Ibrahim, "Mechanical trapping of particles in granular media," *Physical Review E*, vol. 97, p. 022907, 2018.

[28] J. Bridgwater, N. W. Sharpe, and D. C. Stocker, "Particle mixing by percolation," *Transactions of the Institution of Chemical Engineers*, vol. 47, pp. 114–119, 1969.

[29] J. Bridgwater and N. D. Ingram, "Rate of spontaneous inter-particle percolation," *Transactions of the Institution of Chemical Engineers*, vol. 49, no. 3, pp. 163–169, 1971.

[30] D. R. Wilkinson and S. F. Edwards, "Spontaneous interparticle percolation," *Proceedings of the Royal Society of London. Series A, Mathematical and Physical Sciences*, vol. 381, no. 1780, pp. 33–51, 1982.

[31] F. Lominé and L. Oger, "Transport of small particles through a 3D packing of spheres: experimental and nu-

merical approaches," *Journal of Statistical Mechanics: Theory and Experiment*, vol. 2006, no. 07, p. P07019, 2006.

[32] M. Rahman, H. Zhu, A. Yu, and J. Bridgwater, "DEM simulation of particle percolation in a packed bed," *Particuology*, vol. 6, no. 6, pp. 475–482, 2008.

[33] F. Lominé and L. Oger, "Transit time during the interparticle percolation process," *Physical Review E*, vol. 82, p. 041301, 2010.

[34] S. Remond, "DEM simulation of small particles clogging in the packing of large beads," *Physica A: Statistical Mechanics and its Applications*, vol. 389, no. 21, pp. 4485–4496, 2010.

[35] S. Gao, J. M. Ottino, P. B. Umbanhowar, and R. M. Lueptow, "Percolation of a fine particle in static granular beds," *Physical Review E*, vol. 107, p. 014903, 2023.

[36] A. Abdallah, E. Vincens, H. Magoariec, and C. Picault, "DEM filtration modelling for granular materials: Comparative analysis of dry and wet approaches," *International Journal for Numerical and Analytical Methods in Geomechanics*, vol. 48, no. 3, pp. 870–886, 2024.

[37] F. Chen, A. Wautier, P. Philippe, N. Benahmed, and F. Nicot, "Micromechanics of fine-grain infiltration in coarse grain sands," *Acta Geotechnica*, vol. 20, pp. 1533–1548, 2025.

[38] C. Moore and J. Masliyah, "Study in particle percolation: A computer program," *International Journal for Numerical Methods in Engineering*, vol. 6, pp. 25–32, 1973.

[39] J. Masliyah and J. Bridgwater, "Particle percolation: A numerical study," *Transactions of the Institution of Chemical Engineers*, vol. 52, pp. 31–52, 1974.

[40] J. Li, A. Yu, J. Bridgwater, and S. Rough, "Spontaneous inter-particle percolation: A kinematic simulation study," *Powder Technology*, vol. 203, no. 2, pp. 397–403, 2010.

[41] R. H. Davis, J.-M. Serayssol, and E. J. Hinch, "The elastohydrodynamic collision of two spheres," *Journal of Fluid Mechanics*, vol. 163, p. 479–497, 1986.

[42] G. G. Joseph, R. Zenit, M. L. Hunt, and A. M. Rosenwinkel, "Particle–wall collisions in a viscous fluid," *Journal of Fluid Mechanics*, vol. 433, p. 329–346, 2001.

[43] P. Gondret, M. Lance, and L. Petit, "Bouncing motion of spherical particles in fluids," *Physics of Fluids*, vol. 14, no. 2, pp. 643–652, 2002.

[44] C. Ghidaglia, E. Guazzelli, and L. Oger, "Particle penetration depth distribution in deep bed filtration," *Journal of Physics D: Applied Physics*, vol. 24, no. 11, p. 2111, 1991.

[45] C. Ghidaglia, L. de Arcangelis, J. Hinch, and E. Guazzelli, "Hydrodynamic interactions in deep bed filtration," *Physics of Fluids*, vol. 8, no. 1, pp. 6–14, 1996.

[46] B. Muresan, N. Saiyouri, and P.-Y. Hicher, "Dynamic behavior of straining in randomly packed beads: Experimental study," *Journal of Environmental Engineering*, vol. 139, no. 5, pp. 692–702, 2013.

[47] H. Sari, B. Chareyre, E. Catalano, P. Philippe, and E. Vincens, "Investigation of internal erosion processes using a coupled DEM-Fluid method," in *Particle-based Methods II: Fundamentals and Applications* (E. Onate and D. Owen, eds.), pp. 820–830, 2011.

[48] J. Zhao and T. Shan, "Coupled CFD–DEM simulation of fluid–particle interaction in geomechanics," *Powder Technology*, vol. 239, pp. 248–258, 2013.

[49] Z. Xie, S. Wang, and Y. Shen, "CFD-DEM modelling of the migration of fines in suspension flow through a solid packed bed," *Chemical Engineering Science*, vol. 231, p. 116261, 2021.

[50] H. Xiong, Z. Zhang, X. Sun, Z.-Y. Yin, and X. Chen, "Clogging effect of fines in seepage erosion by using CFD–DEM," *Computers and Geotechnics*, vol. 152, p. 105013, 2022.

[51] P. Wang, Q. Li, T. Ma, X. Ou, Y. Shen, Y. Yang, and X. Tian, "An unresolved CFD-DEM method for studying migration and clogging of fine particles through a packed bed," *Ironmaking & Steelmaking*, vol. 50, no. 11, pp. 1618–1630, 2023.

[52] A. Jaiswal, M. D. Bui, and P. Rutschmann, "On the process of fine sediment infiltration into static gravel bed: A CFD–DEM modelling perspective," *River Research and Applications*, vol. 40, no. 1, p. 29 – 48, 2024.

[53] J. A. Dijksman, F. Rietz, K. A. Lőrincz, M. van Hecke, and W. Losert, "Invited Article: Refractive index matched scanning of dense granular materials," *Review of Scientific Instruments*, vol. 83, p. 011301, 01 2012.

[54] P. Aussillous, J. Chauchat, M. Pailha, M. Médale, and E. Guazzelli, "Investigation of the mobile granular layer in bedload transport by laminar shearing flows," *Journal of Fluid Mechanics*, vol. 736, p. 594–615, 2013.

[55] T. Trewhela, C. Ancey, and J. Gray, "An experimental scaling law for particle-size segregation in dense granular flows," *Journal of Fluid Mechanics*, vol. 916, p. A55, 2021.

[56] P. Philippe and M. Badiane, "Localized fluidization in a granular medium," *Physical Review E*, vol. 87, p. 042206, 2013.

[57] F. Brunier-Coulin, P. Cuéllar, and P. Philippe, "Erosion onset of a cohesionless granular medium by an immersed impinging round jet," *Physical Review Fluids*, vol. 2, p. 034302, 2017.

[58] A 2D expression of the norm $u = \sqrt{u_x^2 + u_z^2}$ is used here rather than a 3D expression of the form $u = \sqrt{2u_x^2 + u_z^2}$ (taking advantage of the statistical equivalence between the x and y variables), as the discrepancy between the two expressions is very small (less than 1%).

[59] R. Di Felice, "The voidage function for fluid-particle interaction systems," *International Journal of Multiphase Flow*, vol. 20, no. 1, pp. 153–159, 1994.

[60] J. M. Dallavalle, *Micromeritics: The Technology of Fine Particles, 2nd edition*. Pitman Publishing Corp., London, UK, 1948.

[61] Brass cup lifted by a cam operated via a crank handle.

[62] The tortuosity is evaluated between the point of entry into the porous medium and the end of the trajectory (either trapping or exit from the porous medium in the case of successful percolation), as the ratio between the actual path length – computed from the velocity components assuming identical contributions along x and y – and the straight-line distance.

[63] N. Brodu, J. A. Dijksman, and R. P. Behringer, "Multiple-contact discrete-element model for simulating dense granular media," *Physical Review E*, vol. 91, p. 032201, Mar 2015.

[64] F. Tapia, C.-W. Hong, P. Aussillous, and E. Guazzelli, "Rheology of suspensions of non-brownian soft spheres across the jamming and viscous-to-inertial transitions," *Physical Review Letters*, vol. 133, p. 088201, Aug 2024.

[65] J. R. Smart, S. Beimfohr, and D. T. J. Leighton, "Measurement of the translational and rotational velocities of a noncolloidal sphere rolling down a smooth inclined plane at low reynolds number," *Physics of Fluids A: Fluid Dynamics*, vol. 5, no. 1, pp. 13–24, 1993.

[66] Y. Zhao, K. P. Galvin, and R. H. Davis, "Motion of a sphere down a rough plane in a viscous fluid," *International Journal of Multiphase Flow*, vol. 28, no. 11, pp. 1787–1800, 2002.

[67] R. H. Davis, Y. Zhao, K. P. Galvin, and H. J. Wilson, "Solid–solid contacts due to surface roughness and their effects on suspension behaviour," *Philosophical Transactions of the Royal Society of London. Series A: Mathematical, Physical and Engineering Sciences*, vol. 361, no. 1806, pp. 871–894, 2003.

[68] A. N. Prokunin, "Spherical particle sedimentation along an inclined plane at small reynolds numbers," *Fluid Dynamics*, vol. 33, no. 4, pp. 573–579, 1998.

[69] A. Bazilevskii and A. Rozhkov, "Motion of a sphere down an inclined plane in a viscous flow," *Fluid Dynamics*, vol. 44, p. 566–576, 2009.

[70] G. Barnocky and R. H. Davis, "Elastohydrodynamic collision and rebound of spheres: Experimental verification," *Physics of Fluids*, vol. 31, no. 6, pp. 1324–1329, 1988.

[71] J. Jenkins and M. Koenders, "Hydrodynamic interaction of rough spheres," *Granular Matter*, vol. 7, p. 13–18, 2005.

[72] P. Philippe, "Dataset for "Visco-frictional trapping of particles percolating through a submerged granular medium", `https://doi.org/10.57745/KY6WKR`, Recherche Data Gouv, version 1.0," 2026.